Optics Communications 586 (2025) 131913

Contents lists available at ScienceDirect

Optics Communications

journal homepage: www.elsevier.com/locate/optcom

Phase-compensated differential optical coherence tomography angiography algorithm based on frequency-domain scale-decorrelation information fusion

Kaixuan Hu [a,b], Shujiang Chen [a,b,*], Zhengkai Yao [a,b], Fuwang Wu [a,b], Xiang Pan [a,b], Yongjian Li [a,b], Wei Yi [a,b], Yi Wan [a,b], Weiye Song [a,b,**]

[a] School of Mechanical Engineering, Shandong University, Shandong, Jinan, 250061, China
[b] Key Laboratory of High Efficiency and Clean Mechanical Manufacture of Ministry of Education, Shandong University, Shandong, Jinan, 250061, China

ARTICLE INFO

Keywords:
Optical coherence tomography angiograph
Frequency-domain scale
Decorrelation
Phase difference

ABSTRACT

Optical coherence tomography angiography provides a non-invasive visualization method for retinal microvascular structure. The signal-to-noise ratio and contrast of OCTA images are crucial to distinguish fine capillary networks and depict avascular areas in the retina. In recent years, research on OCTA algorithms has made significant progress in improving image quality. However, there are still some shortcomings. This study proposes an angiography algorithm with frequency domain scale decorrelation fusion by processing and analyzing OCTA images. By analyzing the energy distribution at the frequency domain scale, static background and dynamic blood flow signals can be more accurately distinguished. Through decorrelation at the frequency domain scale, the change of frequency components can be used to enhance the detection of blood flow signals and distinguish blood flow signals from static tissue signals. The results of simulation experiments and in vivo experiments show that the phase-compensated differential angiography algorithm with frequency domain scale decorrelation fusion proposed in this paper not only optimizes the signal-to-noise ratio and contrast of the image, but also effectively reduces noise interference, providing more reliable imaging data support for clinical use.

1. Introduction

Since its initial introduction in the early 1990s, Optical Coherence Tomography (OCT) has evolved into a non-invasive [1], high-resolution three-dimensional imaging technique widely used in various fields such as ophthalmology [2–7], cardiology [8,9], and dermatology [10–12]. An important branch of OCT, Optical Coherence Tomography Angiography (OCTA), uses erythrocytes as contrast agents to visualize vascular networks [13], providing a non-invasive visualization method for retinal microvascular structures. It delivers detailed images of retinal vessels and plays a crucial role in the diagnosis of several eye diseases, including diabetic retinopathy [14–17], age-related macular degeneration (AMD) [18–21], retinal vein occlusion [22], and glaucoma [23,24]. Furthermore, this capability makes it critically important for the early diagnosis of several eye diseases and for tracking disease progression [25].

Despite providing a non-invasive option for retinal angiography, the image quality of OCTA is still influenced by various factors, such as speckle noise and insufficient signal decorrelation [26]. To address these limitations, researchers have developed numerous algorithms aimed at enhancing the quality of angiography. The development and optimization of angiography algorithms are currently prominent topics in OCTA research. Wang et al. proposed an optical microangiography algorithm (OMAG) [27,28] that performes differential operations on complex OCT signals obtained from adjacent B-scans at the same location. This approach incorporats both the phase and amplitude components of the OCT signals into the calculation of blood flow signals, thereby enabling the detection of detailed blood flow and vascular network images and being more sensitive to slow blood flow [29]. The differential phase standard-deviation (DPSD) algorithm developed by Weisong Shi et al. [30], which utilizes the variance in log-scale intensity difference images from consecutive B-scans in the depth direction, enhances the contrast for blood flow, effectively improves the detection capability for low-speed blood flow, especially at the capillary level. Wanrong Gao et al. proposed a differential standard deviation of log-scale intensity

* Corresponding author. School of Mechanical Engineering, Shandong University, Shandong, Jinan, 250061, China.
** Corresponding author. School of Mechanical Engineering, Shandong University, Shandong, Jinan, 250061, China.
E-mail addresses: chsjm@sdu.edu.cn (S. Chen), songweiye@sdu.edu.cn (W. Song).

https://doi.org/10.1016/j.optcom.2025.131913
Received 21 January 2025; Received in revised form 19 April 2025; Accepted 22 April 2025
Available online 22 April 2025

(DSDLI) [31] algorithm that generates en-face angiography by calculating the standard deviation of differential log-scale intensities within a specific depth range, improving both the spatial resolution and the signal-to-noise ratio (SNR) of the images. Jia et al. developed Split-Spectrum Amplitude-Decorrelation Angiography (SSADA) [32] which combines the split-spectrum method with amplitude decorrelation to enhance the contrast of the vascular system, thus maintaining lateral resolution while optimizing the SNR. Mariampillai et al. proposed the speckle variance OCT (SVOCT) algorithm [33,34], which treats the OCT signals as a kind of speckle, where the intensity of the speckle caused by flow is different from that caused by static tissue [35]. By calculating the spot variance signals between B-scans, they more accurately detected microvascular blood flow, significantly improving the sensitivity and image quality of the blood flow signals. Blatter et al. exploited changes in optical path length [36], where the intensity signals of the retinal data collected by the system was changed by the movement of red blood cells. By processing consecutive intensity tomograms, they proposed an angiography algorithm that calculates the squared intensity difference between consecutive tomograms (PID) [37]. Even minor axial displacements of red blood cells yield detectable changes in intensity, allowing methods based on intensity signals to capture a broader dynamic range of flow velocities. With the technological advancements, the quality of OCTA images has significantly improved, allowing physicians to distinguish fine capillary networks and clearly delineate the avascular zone in the retina. However, providing OCTA images with higher SNR and greater contrast remains an important task in current research [38].

This paper proposes a Phase Compensated Differential Interference Frequency Scale (PCD-DIFS) algorithm, which analyzes the energy distribution across the frequency scale to more accurately differentiate between static background signals (tissue information) and dynamic blood flow signals. In frequency domain scale information, low-frequency components typically correspond to slowly changing parts within the image, representing static tissue information changes between different B-scans in OCTA data; high-frequency components typically correspond to rapidly changing parts, representing blood flow signals in OCTA data induced by blood movement between different B-scans. Therefore, reconstructing images between different B-scans in the frequency domain for angiography can effectively suppress background signals. By decorrelating in the frequency domain, the variation in frequency components can be used to enhance the detection of blood flow signals, distinguishing blood flow signals from static tissue signals, and improving the SNR and contrast of OCTA images. Applied to retinal OCTA imaging, this algorithm verifies its performance advantages in retinal angiography.

2. Methods

2.1. Theory of PCD-DIFS

We propose a Phase Compensation Differential for Decorrelation Information Fusion in Frequency Domain Scale (PCD-DIFS) algorithm based on frequency domain scale decorrelation information fusion for optical coherence tomography angiography (OCTA), which enhances the SNR of OCTA images, suppresses tissue information in OCTA images, and improves the detection capabilities for microvasculature. The principle is as follows:

The interference signals are acquired using a high-speed, high-resolution, broadband near-infrared OCTA system according to the scanning protocol described in the previous section. Subsequently, the interference signals undergo Fourier transformation to produce three-dimensional OCTA data, which the PCD-DIFS algorithm is applied. Fig. 1 illustrates the data processing workflow of the PCD-DIFS algorithm.

Initially, the n and $n+1$ scan images at position k ($k = 1,2,3, \ldots, K$) are selected from all $3D$ OCTA data, where n ranges from 1 to N, the number of repeat scans at position k. Image reconstruction is then performed using the data from the n B-scan and the $n+1$ B-scan. Respiratory or cardiac motion can cause phase shifts, necessitating the calculation of phase offsets for alignment, represented as:

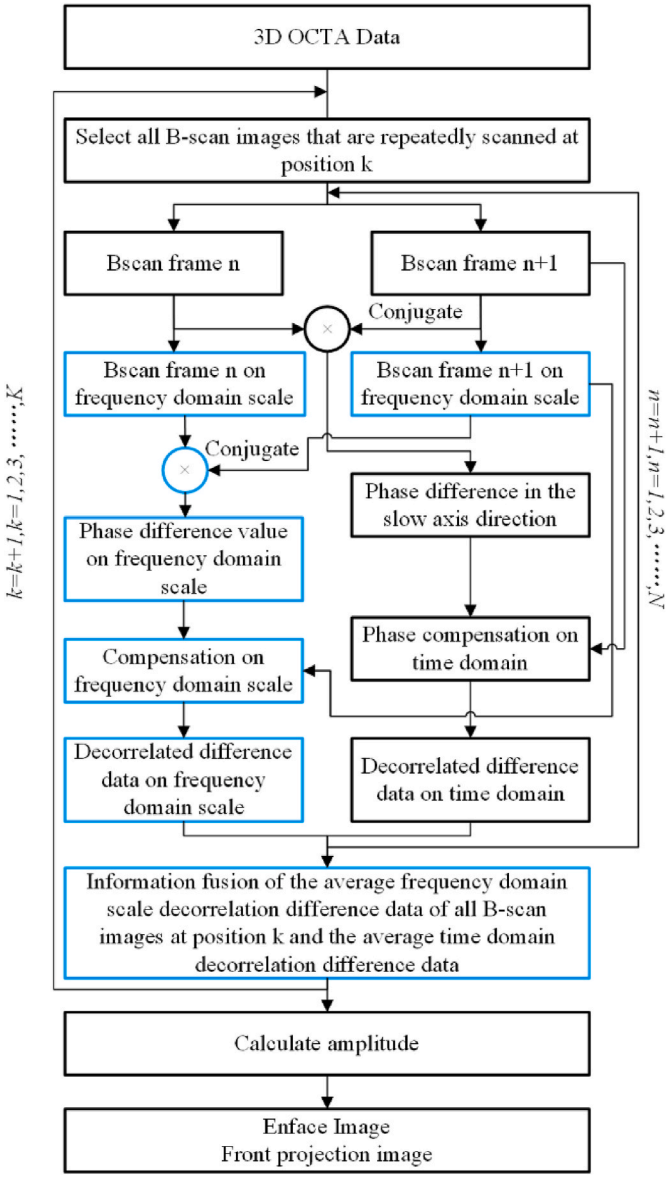

Fig. 1. PCD-DIFS algorithm flow chart.

$$C_{i,j,n+1} = B_{i,j,n+1}B^{*}_{i,j,n} \tag{1}$$

where B and C respectively represent the original $3D$ data and the $3D$ data obtained by complex conjugate multiplication of the n B-scan data with the $n+1$ B-scan data. i represents the pixel index in the A-scan depth direction, j represents the pixel index in the fast-axis B-scan direction, and n represents the index of the repeat scan at position k.

The complex phase offset φ in the j direction is calculated for the obtained C data, where M is the number of pixels in the depth of the A scanning direction. The calculation formula is as follows:

$$\varphi = -\frac{1}{M}tan^{-1}\left(\frac{Im\left(\sum_{i=1}^{M} C_{i,j,n+1}\right)}{Re\left(\sum_{i=1}^{M} C_{i,j,n+1}\right)}\right) \tag{2}$$

$$B'_{i,j,n+1} = B_{i,j,n+1}\, exp(i\varphi) \tag{3}$$

B' represents the phase-compensated complex data, correcting for phase changes caused by object movement. The temporal decorrelation differential data can be obtained by the formula:

$$T_{angio_{i,j,k}} = \frac{1}{N-1}\sum_{n=1}^{N-1}\left|B'_{i,j,n+1} - B_{i,j,n}\right| \tag{4}$$

T represents the average amplitude of the temporal decorrelation phase compensation differential data between the N scans at position k, highlighting changes especially dynamic information in the blood flow signals, and emphasizing areas with strong blood flow signals.

In the frequency domain, low-frequency components typically correspond to slowly changing parts within the image, representing static tissue information changes between different B-scans in OCTA data; high-frequency components generally correspond to rapidly changing parts, representing changes caused by blood flow between different B-scans. Image reconstruction between different B-scans in the frequency domain scale can thus produce images that suppress background tissue signals. Computation process is as follows:

$$F_{u,v,w} = FFT\left(B_{i,j,n}\right)$$

$$F_{u,v,w+1} = FFT\left(B_{i,j,n+1}\right) \tag{5}$$

Perform a dual Fourier transform on the data from the nth B scan at position k and the data from the $n+1$ B scan to extract the frequency domain scale information. F represents the frequency domain scale data after the Fourier transform of the original B data, and u, v, and w correspond to i, j, and n respectively.

$$\varphi' = -\frac{1}{U}tan^{-1}\left(\frac{Im\left(\sum_{u=1}^{U}F_{u,v,w+1}\right)}{Re\left(\sum_{u=1}^{U}F_{u,v,w+1}\right)}\right) \tag{6}$$

The frequency domain scale phase offset φ' in the v direction is calculated for the obtained F data, where U is the index of the frequency domain scale data F in the first dimension.

$$F'_{u,v,w+1} = F_{u,v,w+1}\, \exp(i\varphi') \tag{7}$$

F' represents the frequency domain scale data after phase compensation in the frequency domain scale, and the frequency domain scale decorrelation differential data is obtained by the formula:

$$P_{angio_{i,j,k}} = \frac{1}{W-1}\sum_{w=1}^{w-1}\left|\left(\frac{1}{MV}\sum_{u=1}^{M}\sum_{v=1}^{V}\left(F'_{u,v,w+1} - F_{u,v,w}\right)exp\left(i2\pi\left(\frac{ui}{M}+\frac{vj}{V}\right)\right)\right)\right| \tag{8}$$

P represents the frequency domain scale data after decorrelation phase difference, and finally the PCD-DIFS data can be represented as:

$$I_{angio_{i,j,K}} = \sum_{k=1}^{K}\frac{T_{angio_{i,j,k}} + P_{angio_{i,j,k}}}{2} \tag{9}$$

I is the final output data fusing temporal and frequency domain scale decorrelation phase difference information.

By iteratively processing data at all k positions, all acquired data can be computed, and the amplitude of all data projected in the depth direction produces the OCTA en-face projection image.

This paper uses five other algorithms (OMAG, DPSD, DSDLI, SVOCT, PID) to calculate angiographic images on the same OCTA dataset for comparison. The dynamic signals of these five methods are expressed as:

$$OMAG_{i,j} = \frac{1}{N-1}\sum_{n=1}^{N-1}\left|B'_{i,j,n+1} - B_{i,j,n}\right| \tag{10}$$

$$DL_{i,j,n} = L_{i,j,n+1} - L_{i,j,n} \tag{11}$$

$$DSDLI_{i,j,n} = \sqrt{\frac{1}{L}\sum_{i=i_0}^{i_0+L-1}\left(DL_{i,j,n} - \frac{1}{L}\sum_{i=l}^{M+l-1}DL_{i,j,n}\right)^2} \tag{12}$$

$$DPSD_{i,j,n} = \sqrt{\frac{1}{L}\sum_{i=i_0}^{i_0+L-1}\left(P'_{i,j,n} - P'_{mean\,j,n}\right)^2} \tag{13}$$

$$SVOCT_{i,j} = \sqrt{\frac{1}{N}\sum_{n=1}^{N}\left(\left|B_{i,j,n}\right| - \frac{1}{N}\sum_{n=1}^{N}\left|B_{i,j,n}\right|\right)^2} \tag{14}$$

$$PID_{i,j,k} = \sum_{k=1}^{K}\left(20\log\left(\left|B'_{i,j,n}\right|\right) - 20\log\left(\left|B_{i,j,n+1}\right|\right)\right)^2 \tag{15}$$

where, $L_{i,j,n+1}$ represents the logarithmic scale structure image of $B'_{i,j,n+1}$, $L_{i,j,n}$ represents the logarithmic scale structure image of $B_{i,j,n}$, L and $i_0 + L - 1$ represent the starting point and end point of a given depth, that is, a pixel window of size L; $P_{i,j,n}$ is the differential phase image of the data after phase offset compensation, $P'_{i,j,n}$ is the phase difference image after removing random noise.

2.2. OCTA imaging systems

The raw data were acquired at an A-scan rate of 250 kHz using a spectral domain OCT (SD-OCT) system developed in our laboratory [39], as shown in Fig. 2.

A superluminescent diode (SLD) light source and a high-speed line scan camera (Octoplus, e2v, Teledyne, UK) were used. The central wavelength of the system was 853.5 nm, the spectral width was 145 nm, the axial resolution of the system was actually measured to be 2.3 μm, the roll-off was 5.7 dB at 1.2 mm, and the roll-off was about 11.88 dB at 2 mm. When the A-scan rate was 250 kHz, the detection sensitivity was 99.95 dB.

3. Result

3.1. Evaluation indicators

In order to quantitatively compare the performance of PCD-DIFS with other algorithms, the following common indicators are used for evaluation. The SNR and contrast-to-noise ratio (CNR) of dynamic blood flow signals and static signals are calculated [30]. The specific calculation formula is as follows:

$$SNR = 20\,log\left(\frac{M_{flow}}{\sigma_{static}}\right) \tag{16}$$

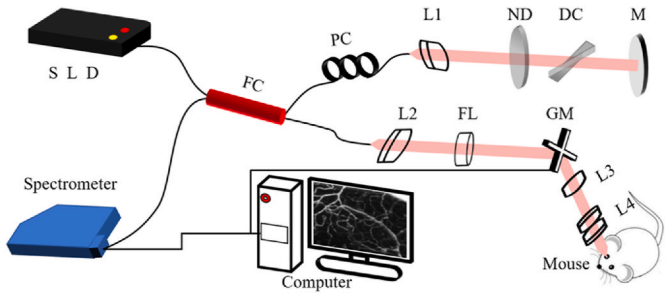

Fig. 2. The High-speed OCTA system. SLD: super luminescent diode; FC: fiber coupler; PC: polarization controller; L1, L2: collimating lens; ND: neutral density filter; DC: dispersion controller; M: mirror; FL: focus tunable lens; GM: two-dimensional scanning galvanometer; L3: achromatic doublet lens; L4: two achromatic doublet lens.

$$CNR = \frac{M_{flow} - M_{static}}{\sigma_{static}} \quad (17)$$

Where M_{flow} represents the average value of the selected blood flow signal area, M_{static} represents the average value of the selected static signal area, and σ_{static} represents the standard deviation of the selected static signal area. SNR represents the SNR of the image. The larger the value, the better the image quality. CNR represents the contrast-to-noise ratio, where larger values indicate reduced background noise and enhanced image quality.

3.2. Animal preparation

In the retinal imaging experiments, healthy 8-week-old male black mice (C57BL/6) were selected for OCTA imaging. The experimental procedures were approved by the school ethics committee (approval number 240008). All animal care and experimental procedures adhered to ethical standards. The mice were fixed on the experimental table and anesthetized continuously with an anesthesia mask. The isoflurane concentration in the anesthesia mask ranged from 2 to 3 %, and the oxygen flow rate was maintained at 150–250 mL/min. Tropicamide (1 %) eye drops were given to dilate the pupils, and eye drops were used to keep the eyes moist during the experiment. A heating pad was used to maintain the body temperature of the mice during the experiment.

3.3. Computational complexity

To comprehensively evaluate the computational efficiency of the method proposed in this study, we conducted a comparative analysis of the computational complexity of various algorithms. Computational complexity is a fundamental theoretical metric for assessing algorithmic performance. It primarily includes two aspects: time complexity and space complexity, which describe the amount of computational resources required by an algorithm as the input size scales. Big-O notation is commonly used to represent these complexities.

After importing the data using a standardized procedure, the theoretical computational complexity is derived based on the core processing steps of each algorithm by analyzing the types of operations involved, decomposing each module into its basic operations, and expressing the overall complexity using Big-O notation. The results are summarized in Table 1T denotes the number of scanning positions; F represents the total number of B-scans, calculated as the number of scanning positions multiplied by the number of repeated scans at each position; A is the number of A-scans per B-scan; D denotes the image reconstruction depth; N_D refers to the sliding window size in the DPSD algorithm; and N_L is the sliding window size in the DSDLI algorithm.

According to the complexity analysis, the time complexity of most algorithms is primarily dominated by the Fourier transform and per-frame processing. Both OMAG and PID exhibit time complexity of $O(T{\cdot}F{\cdot}A{\cdot}D)$. In contrast, DPSD and DSDLI introduce sliding windows into their processing pipelines, leading to increased time complexity of $O(T{\cdot}F{\cdot}A{\cdot}D{\cdot}N_D)$ and $O(T{\cdot}F{\cdot}A{\cdot}D{\cdot}N_L)$, respectively. SVOCT involves a squared term in the number of B-scans, resulting in a complexity of $O(T{\cdot}F^2{\cdot}A{\cdot}D)$, while the proposed PCD-DIFS algorithm has a time complexity of $O(T{\cdot}F{\cdot}A{\cdot}D{\cdot}log(A{\cdot}D))$ due to the use of two-dimensional Fourier transforms. In terms of space complexity, all algorithms exhibit similar memory requirements, primarily determined by the need to store frame data and intermediate results. Thus, the memory footprint increases linearly with T, A, and D.

Table 1
Comparison of computational complexity.

Algorithm	Time Complexity	Space Complexity
OMAG	$O(T{\cdot}F{\cdot}A{\cdot}D)$	$O(A{\cdot}F{\cdot}D)$
DPSD	$O(T{\cdot}F{\cdot}A{\cdot}D{\cdot}N_D)$	$O(A{\cdot}F{\cdot}(D-N_D))$
DSDLI	$O(T{\cdot}F{\cdot}A{\cdot}D{\cdot}N_L)$	$O(A{\cdot}F{\cdot}(D-N_L))$
SVOCT	$O(T{\cdot}F^2{\cdot}A{\cdot}D)$	$O(A{\cdot}F{\cdot}D)$
PID	$O(T{\cdot}F{\cdot}A{\cdot}D)$	$O(A{\cdot}F{\cdot}D)$
PCD-DIFS	$O(T{\cdot}F{\cdot}A{\cdot}D{\cdot}log(A{\cdot}D))$	$O(A{\cdot}F{\cdot}D)$

Although the PCD-DIFS algorithm has slightly higher time complexity than other methods, it offers a key advantage by concentrating image processing in the frequency domain via two-dimensional Fourier transforms. This allows for more efficient extraction of image features and finer detail preservation. Compared to traditional one-dimensional Fourier transforms, 2D transforms process both horizontal and vertical frequency components simultaneously, making them particularly suitable for image reconstruction and noise reduction. Moreover, since the space complexity of PCD-DIFS remains comparable to that of other algorithms, it enables more sophisticated frequency-domain operations without significant additional memory consumption.

3.4. In vivo retinal images

In order to compare the performance of the algorithms more specifically, the left area in the optic nerve head of healthy mice was scanned to test the performance of the PCD-DIFS algorithm. The system's Aline scanning frequency was set to 250 kHz. In order to better demonstrate the contrast between blood vessels and background and calculate the signal-to-noise ratio, the scanning protocol was set to: $Nrep = 4$, $\triangle T = 4$ ms, that is, the number of Alines per frame was 200, $\Sigma A\text{-}line = 0.31\ \mu m^{-1}$. The six algorithms were all performed on the same OCT data. Fig. 3 shows the angiography images of the six algorithms at the same B-scan position with the same data set.

By comparing Fig. 3, it can be observed that PCD-DIFS obtains the best vascular signal intensity on the B-scan image and suppresses the retinal tissue background well. Compared with DSDLI, SVOCT and PID, the retinal tissue background area is better suppressed, and stronger signals are shown at the location of the blood vessels. A vertical line is drawn in the same area (red line area), and the signals within this region are extracted and illustrated in Fig. 3(g), with the signal intensity of the tissue-free area aligned to the average value. It can be observed from the vascular intensity signals at the same position that PCD-DIFS obtains the highest intensity signal at the vascular position. At the same time, in the tissue background area, PCD-DIFS exhibits the smallest fluctuation and more effectively suppresses background noise.

In the optic nerve head area, we selected a rectangular area containing capillaries (red rectangle). Through the analysis of the local magnified image, we can clearly observe the significant advantages of the PCD-DIFS algorithm in suppressing image artifacts and background signals, as shown in Fig. 4. This algorithm can effectively reduce the interference of background noise on capillary signals, thereby presenting the details of the vascular structure more clearly. In contrast, other algorithms exhibit varying degrees of deficiencies when processing capillary areas.

The OMAG algorithm displays significant artifact noise in the background tissue area, which will mask part of the vascular signals and affect the visualization of the vascular signals, as shown in Fig. 4(b). The DPSD and DSDLI algorithms are prone to artifacts in areas with dense capillaries, resulting in the inability to fully display the details of the capillary signals, as shown in Fig. 4(c) and (d). The presence ofthess artifacts weakens the SNR of the images and reduce the resolution of the blood vessels. In addition, there is obvious stripe noise in the image of the SVOCT algorithm. The noise interferes with the expression of capillary signals, destroying the continuity and detail of the capillary structure, as shown in Fig. 4(e). Although the PID method can extract capillary signals to a certain extent, there are still obvious ghosts in the angiography it generates, which affects the authenticity and recognizability of the capillary signals, as shown in Fig. 4(f). Through the comparative analysis of local capillary detail images, the superiority of the PCD-DIFS algorithm can be fully demonstrated. It can more effectively suppress artifacts and noise in background tissue, while reducing the interference of stripe noise on vascular signals. Such performance

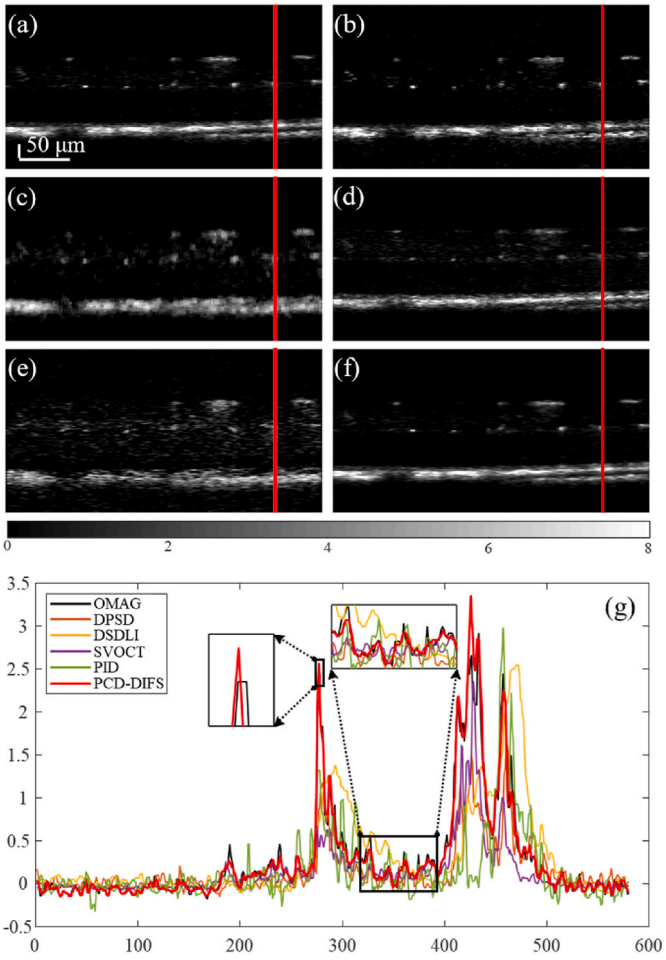

Fig. 3. Bscan signal intensity comparison chart. (a) OMAG. (b) DPSD. (c) DSDLI. (d) SVOCT. (e) PID. (f) PCD-DIFS. (g) Blood vessel intensity signals at the same location (red line) (a)~(f) share the same scale bar.

makes the PCD-DIFS algorithm have significant advantages in improving the display of capillary details and improving the SNR and contrast of images. This ability not only helps to analyze capillary structures more accurately, but also provides more reliable data support for the research and diagnosis of ophthalmic diseases.

In the green area in Fig. 4, a total of 2250 pixels were extracted, including 870 pixels from the capillary area and 1380 pixels from the background tissue area. By analyzing the intensity distribution of these pixels, an intensity map is drawn as shown in Fig. 5. It can be observed from the local area intensity map that the PCD-DIFS algorithm performs well in the capillary area, achieving a SNR of 23.35 dB, the highest among the six algorithms. The pixel signal intensity in the capillary area has achieved the best value, which is significantly higher than that of other algorithms. Additionally, the fluctuations in the intensity signals within the background tissue area is smaller, indicating that PCD-DIFS can more effectively balance the relationship between signal enhancement and noise suppression. Although the OMAG and DPSD algorithms have lower mean signal intensity in the background tissue area and show stronger background noise suppression ability, this also leads to a greater loss of signal intensity in the capillary area, rendering them less effective for extracting microvascular signals compared to the PCD-DIFS algorithm. Through the analysis of the intensity map of the local area, provides a more intuitive representation of the performance differences among the algorithms in the capillary area, further highlighting the PCD-DIFS algorithm's superior ability to enhance vascular signals while suppressing background noise, making it a better choice for improving the capillary signal intensity value and suppressing the background

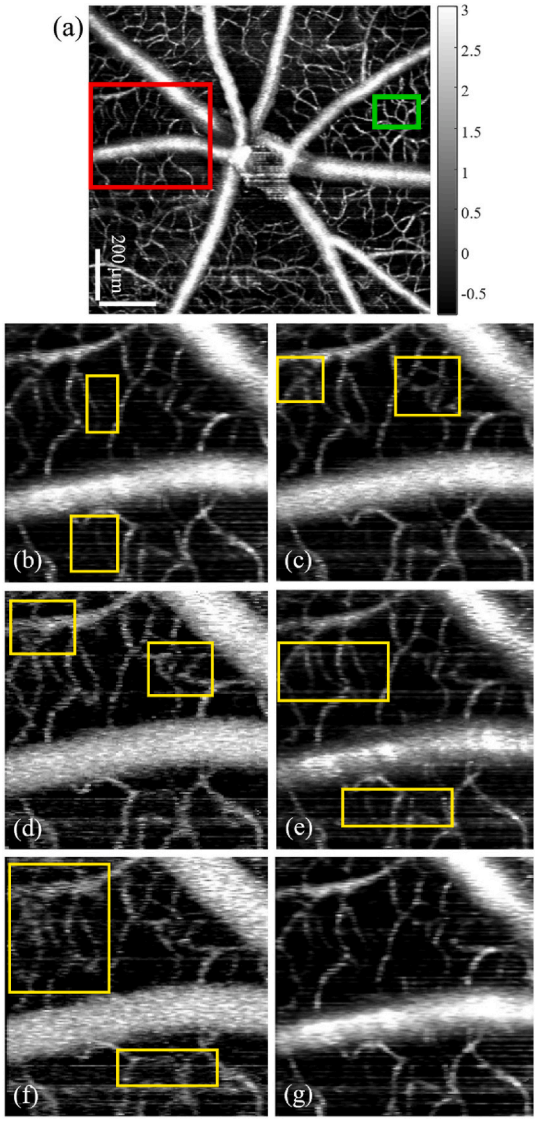

Fig. 4. Local detail of retinal images. (a) Frontal projection image of the optic nerve head. (b) OMAG. (c) DPSD. (d) DSDLI. (e) SVOCT. (f) PID. (g) PCD-DIFS.

tissue signal.

Fig. 6(a)–(f) shows the frontal projection images generated by the retina of the six algorithms. The red area denotes the selected vascular, and the blue area indicates the background tissue, which is used to calculate the SNR and CNR of the local area. The global threshold is automatically determined using the Otsu method to segment the global blood vessels from the background tissue. The threshold is then applied to the grayscale image of the frontal projection of the retina to perform binarization, resulting a binary image where white (value 1) represents the vascular area and black (value 0) represents the background area. The mean and standard deviation of the signal intensity for the vascular area and the background tissue area are calculated respectively, and the global SNR and CNR are calculated. The SNR and contrast statistics for the local and global areas are shown in Fig. 6(g). In terms of the local capillary SNR, PCD-DIFS achieves the best SNR and contrast, with an SNR of 25.31 dB, which is 3.54 dB higher than the average of the other five algorithms, as well as a CNR of 13.19 dB, which is 1.15 dB higher than the average of the other five algorithms. In the capillary area, the PCD-DIFS algorithm can better enhance the capillary signal intensity, while suppressing signals from the retinal tissue, thereby better improving the contrast between the vascular area and the background tissue area.

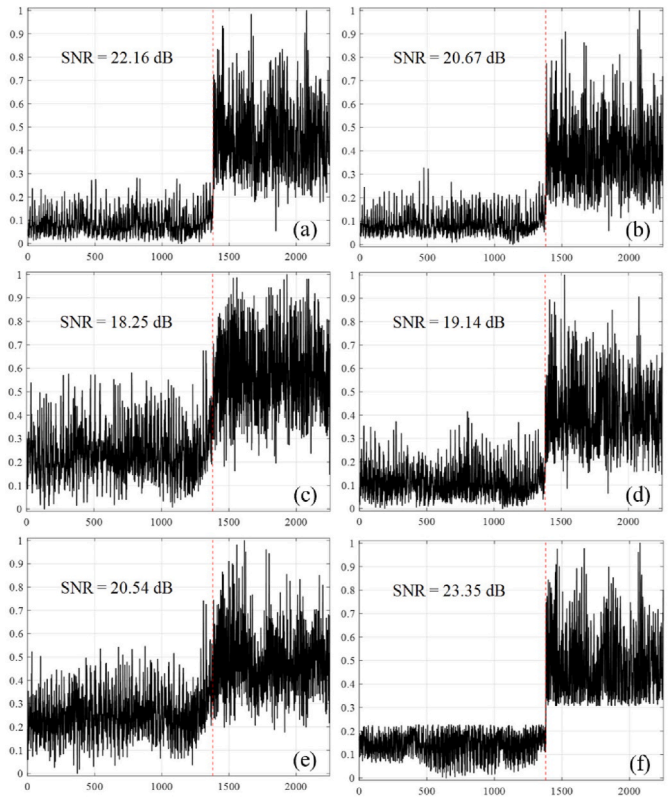

Fig. 5. Signal SNR curve of the local (green rectangular box) signals of the retinal image. (a) OMAG. (b) DPSD. (c) DSDLI. (d) SVOCT. (e) PID. (f) PCD-DIFS.

Fig. 7 shows the frontal projection of the retina in the mouse optic nerve head area. A comparison of these images revealed that the vascular area signal extraction from DPSD, DSDLI and OMAG images showed a degree of unevenness, resulting in reduced visualization of blood vessels in the foveal area. Both SVOCT and PID performed poorly for the signal intensity of microvessels. PCD-DIFS can achieve better contrast and better extract vascular signals for both capillary and large blood vessel areas. The global SNR and contrast of the optic nerve head area were calculated for quantitative comparison, and the results are shown in Fig. 7(g) and (h). Compared to the OMAG algorithm, the SNR of PCD-DIFS imaging results increased by an average of 1.77 dB and the CNR increased by an average of 0.87 dB.

4. Conclusion

In recent years, research on OCTA algorithms has made significant strides in the image analysis of fundus diseases. This study explored the application of the PCD-DIFS with frequency-domain scale decorrelation information fusion in OCTA by processing and analyzing OCTA images. This approach has significantly improved the SNR and contrast of the images, while suppressing background tissue information, thereby enhancing the visualization of vascular signals, and improving the accuracy of lesion detection.

By comparing and analyzing the performance of various algorithms, the results indicate that PCD-DIFS has significant advantages in vascular signal extraction and background noise suppression. In B-scan images, the PCD-DIFS algorithm can achieve the highest vascular signal intensity and effectively suppress the background noise from retinal tissue. At vascular locations, the signal intensity of PCD-DIFS is significantly higher than that of other algorithms, while in the background area, its volatility is the lowest, showing a stronger ability to suppress background noise. In addition, in detailed images of the capillary area, the

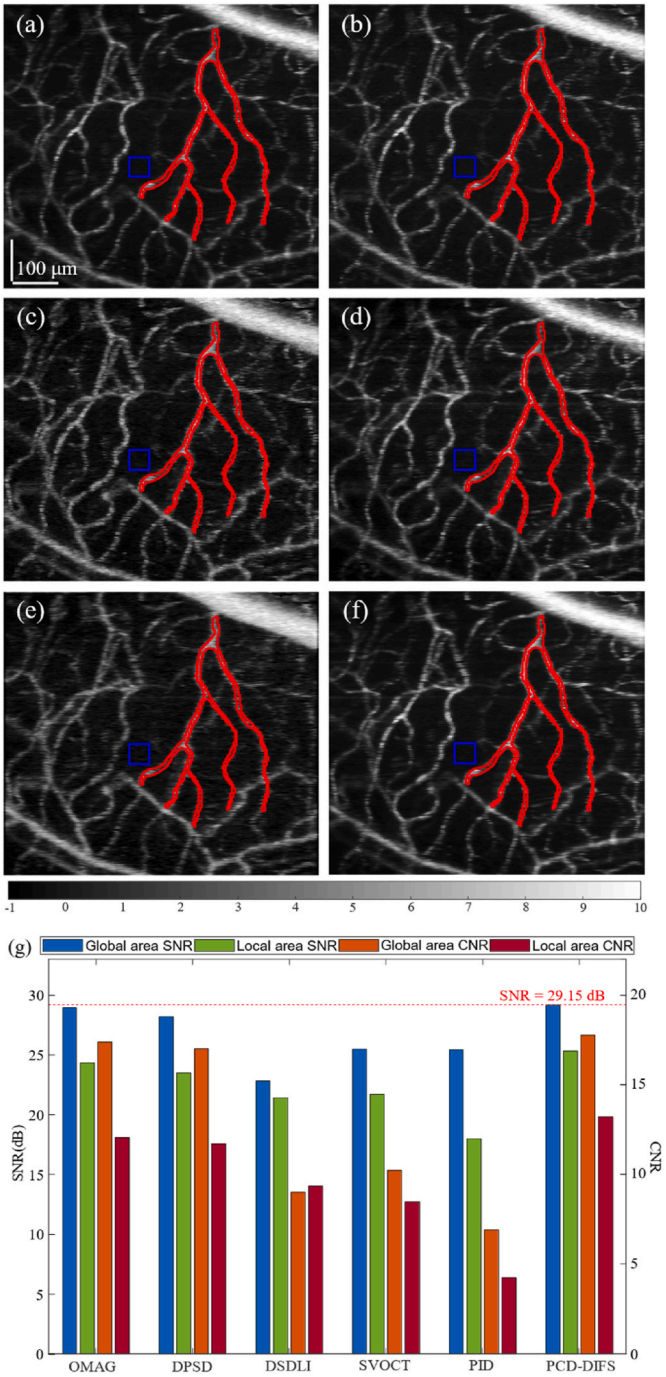

Fig. 6. Retinal images and comparison of local and global signal intensity. (a) OMAG. (b) DPSD. (c) DSDLI. (d) SVOCT. (e) PID. (f) PCD-DIFS. (g) Comparison of local and global SNR and CNR intensity. (a)~(f) share the same scale bar.

PCD-DIFS algorithm effectively reduces the interference from artifacts and streak noise, resulting in a clearer representation of vascular signals.

PCD-DIFS demonstratedthe best performance in both local and global SNR and CNR analyses of mouse retinal frontal projection images. In the local capillary region, PCD-DIFS achieved an SNR of 25.31 dB and a CNR of 13.19 dB, which were, on average, 3.54 dB and 1.15 dB higher, respectively, than the other five algorithms. In addition, PCD-DIFS performed better than other algorithms in the optic nerve head area. The vascular area signal extraction from DPSD, DSDLI and OMAG images exhibited a degree of inhomogeneity, resulting in reduced visualization of blood vessels in the foveal area. Furthermore, SVOCT and PID demonstrated poor performance regarding the signal intensity of

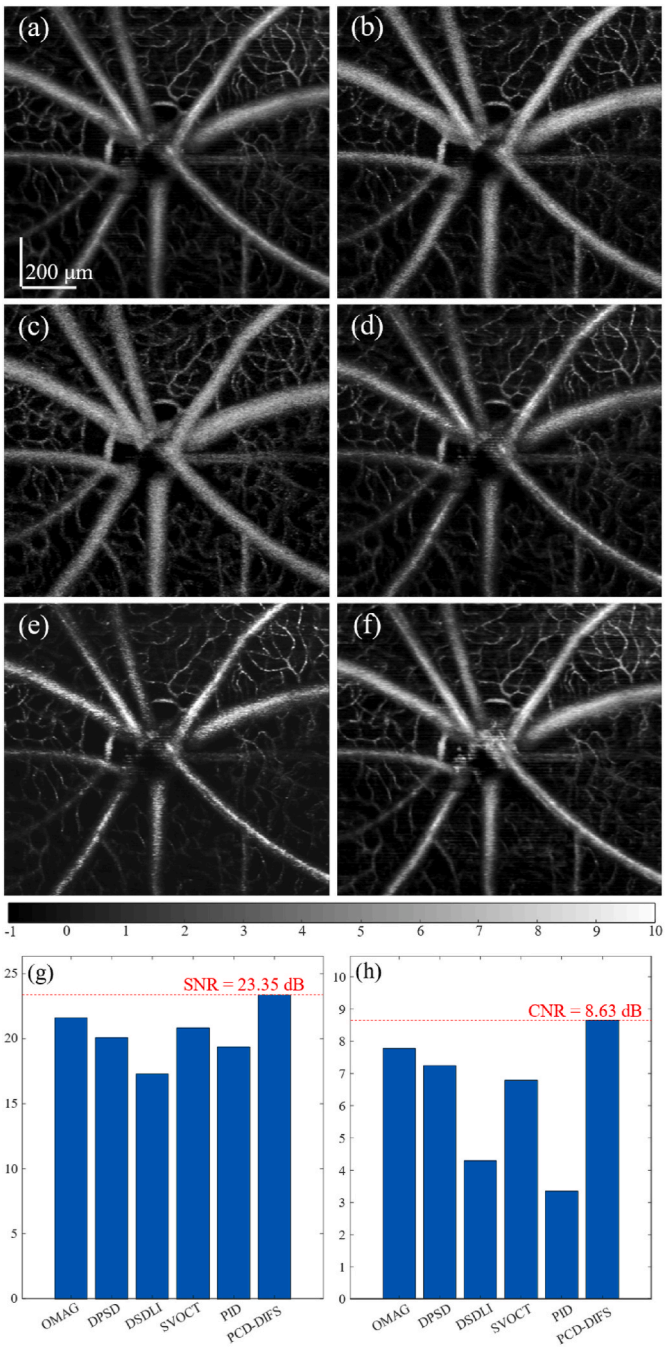

Fig. 7. Optic nerve head image and global intensity signal map. (a) OMAG. (b) DPSD. (c) DSDLI. (d) SVOCT. (e) PID. (f) PCD-DIFS. (g) Global SNR intensity. (h) Global CNR intensity. (a)~(f) share the same scale bar.

microvessels, whereas PCD-DIFS can better improve the SNR and contrast of the vascular area by enhancing the vascular signal and suppressing the background artifacts. The results indicate that compared to the OMAG algorithm, the PCD-DIFS algorithm has an average SNR increase of about 1.77 dB and a CNR increase of about 0.87 dB in the optic nerve head area. Compared to the other five algorithms, PCD-DIFS algorithm has an average SNR increase of about 3.53 dB and a CNR increase of about 2.75 dB in the optic nerve head area.

The in vivo experimental results demonstrate that, compared to traditional methods, the PCD-DIFS algorithm not only optimizes the SNR of the image, but also effectively reduces noise interference, thereby providing more reliable imaging data for clinical use. Based on the above results, the PCD-DIFS algorithm effectively improves the extraction ability of blood flow signals while suppressing background tissue and artifact noise through the introduction of decorrelated information fusion at the frequency domain scale. This improvement not only elevates the quality of OCTA images, but also provides a reliable method for the accurate detection of microvascular signals. The algorithm holds substantial clinical application potential for the diagnosis and grading evaluation of complex lesions, while simultaneously presenting new research ideas and directions for the advanced application of OCTA imaging technology in the medical field.

CRediT authorship contribution statement

Kaixuan Hu: Writing – original draft, Visualization, Validation, Project administration, Methodology, Formal analysis, Data curation, Conceptualization. **Shujiang Chen:** Writing – review & editing, Supervision, Conceptualization. **Zhengkai Yao:** Writing – review & editing, Writing – original draft, Formal analysis. **Fuwang Wu:** Methodology, Formal analysis, Data curation. **Xiang Pan:** Visualization, Software, Project administration. **Yongjian Li:** Resources, Data curation. **Wei Yi:** Resources, Funding acquisition. **Yi Wan:** Writing – review & editing, Supervision, Funding acquisition. **Weiye Song:** Writing – review & editing, Supervision, Resources, Project administration, Funding acquisition, Data curation, Conceptualization.

Declaration of competing interest

The authors declare that they have no known competing financial interests or personal relationships that could have appeared to influence the work reported in this paper.

Acknowledgments

This research was supported by the National Natural Science Foundation of China (62205181); the Natural Science Foundation of Shandong Province (ZR2022QF017); the Shandong Province Outstanding Youth Science Fund Project (Overseas) (2023HWYQ-023); the Taishan Scholar Foundation of Shandong Province (tsqn202211038); the National Natural Science Foundation of China (51975336); the Key Technology Research and Development Program of Shandong Province (2020JMRH0202); the Key Technology Research and Development Program of Shandong Province (2022CXGC020701); the Shandong Province New Old Energy Conversion Major Industrial Tackling Projects (2021–13).

Data availability

Data will be made available on request.

References

[1] D. Huang, E.A. Swanson, C.P. Lin, J.S. Schuman, W.G. Stinson, W. Chang, M. R. Hee, T. Flotte, K. Gregory, C.A. Puliafito, J.G. Fujimoto, Optical coherence tomography, Science 254 (1991) 1178–1181, https://doi.org/10.1126/science.1957169.

[2] J. Wang, W. Song, N. Sadlak, M.G. Fiorello, D. Manishi, J. Yi, Oxygen saturation of macular vessels in glaucoma subjects using visible light optical coherence tomography, Investig. Ophthalmol. Vis. Sci. 64 (2023) 1357.

[3] J. Wang, S. Nolen, W. Song, W. Shao, W. Yi, A. Kashani, J. Yi, A dual-channel visible light optical coherence tomography system enables wide-field, full-range, and shot-noise limited human retinal imaging, Commun. Eng. 3 (2024) 1–13. https://www.nature.com/articles/s44172-024-00167-7.

[4] J. Wang, W. Song, N. Sadlak, M.G. Fiorello, M. Desai, J. Yi, Retinal parafoveal oximetry using visible light optical coherence tomography in health subjects, in: Ophthalmic Technologies XXXIII, SPIE, 2023, p. PC1236002, https://doi.org/10.1117/12.2648449.

[5] X. He, W. Song, Y. Wang, F. Poiesi, J. Yi, M. Desai, Q. Xu, K. Yang, Y. Wan, Lightweight retinal layer segmentation with global reasoning, IEEE Trans. Instrum. Meas. 73 (2024) 1–14, https://doi.org/10.1109/TIM.2024.3400305.

[6] X. He, Y. Wang, F. Poiesi, W. Song, Q. Xu, Z. Feng, Y. Wan, Exploiting multi-granularity visual features for retinal layer segmentation in human eyes, Front.

Bioeng. Biotechnol. 11 (2023) 1191803. https://www.frontiersin.org/articles/10.3389/fbioe.2023.1191803/full.

[7] Q. Xu, X. He, M. Xu, K. Hu, W. Song, A Dual-branch Multidomain Feature Fusion Network for axial super-resolution in optical coherence tomography, IEEE Signal Process. Lett. 32 (2025) 461–465. https://ieeexplore.ieee.org/abstract/document/10771640.

[8] T. Yonetsu, K. Wakabayashi, T. Mizukami, M.H. Yamamoto, S. Yasuhara, S. Kondo, Y. Oishi, T. Okabe, T. Sugiyama, M. Araki, M. Takano, N. Kobayashi, S. Kimura, Y. Yamakami, S. Suwa, S. Nakamura, S. Mitomo, T. Kakuta, E. Usui, T. Higuma, J. Ako, Y. Minami, M. Iwasaki, J. Shite, A. Kozuki, S. Saito, K. Shishido, H. Okura, G. Naruse, S. Uemura, T. Kume, M. Nanasato, T. Dohi, T. Ashikaga, H. Otake, H. Mori, T. Sekimoto, Y. Sugizaki, T. Shinke, Optical coherence tomography–guided percutaneous coronary intervention for ST-segment elevation myocardial infarction: rationale and design of the ATLAS-OCT study, Am. J. Cardiol. 203 (2023) 466–472, https://doi.org/10.1016/j.amjcard.2023.07.077.

[9] H.R. Reynolds, A. Maehara, R.Y. Kwong, T. Sedlak, J. Saw, N.R. Smilowitz, E. Mahmud, J. Wei, K. Marzo, M. Matsumura, A. Seno, A. Hausvater, C. Giesler, N. Jhalani, C. Toma, B. Har, D. Thomas, L.S. Mehta, J. Trost, P.K. Mehta, B. Ahmed, K.R. Bainey, Y. Xia, B. Shah, M. Attubato, S. Bangalore, L. Razzouk, Z.A. Ali, N. B. Merz, K. Park, E. Hada, H. Zhong, J.S. Hochman, Coronary optical coherence tomography and cardiac magnetic resonance imaging to determine underlying causes of myocardial infarction with nonobstructive coronary arteries in women, Circulation 143 (2021) 624–640, https://doi.org/10.1161/CIRCULATIONAHA.120.052008.

[10] B. Wan, C. Ganier, X. Du-Harpur, N. Harun, F.M. Watt, R. Patalay, M.D. Lynch, Applications and future directions for optical coherence tomography in dermatology, Br. J. Dermatol. 184 (2021) 1014–1022, https://doi.org/10.1111/bjd.19553.

[11] H.D. Heibel, L. Hooey, C.J. Cockerell, A review of noninvasive techniques for skin cancer detection in dermatology, Am. J. Clin. Dermatol. 21 (2020) 513–524, https://doi.org/10.1007/s40257-020-00517-z.

[12] F. Latriglia, J. Ogien, C. Tavernier, S. Fischman, M. Suppa, J.-L. Perrot, A. Dubois, Line-field confocal optical coherence tomography (LC-OCT) for skin imaging in dermatology, Life 13 (2023) 2268, https://doi.org/10.3390/life13122268.

[13] R.F. Spaide, J.G. Fujimoto, N.K. Waheed, S.R. Sadda, G. Staurenghi, Optical coherence tomography angiography, Prog. Retin. Eye Res. 64 (2018) 1–55, https://doi.org/10.1016/j.preteyeres.2017.11.003.

[14] Z. Sun, D. Yang, Z. Tang, D.S. Ng, C.Y. Cheung, Optical coherence tomography angiography in diabetic retinopathy: an updated review, Eye 35 (2021) 149–161, https://doi.org/10.1038/s41433-020-01233-y.

[15] N.K. Waheed, R.B. Rosen, Y. Jia, M.R. Munk, D. Huang, A. Fawzi, V. Chong, Q. D. Nguyen, Y. Sepah, E. Pearce, Optical coherence tomography angiography in diabetic retinopathy, Prog. Retin. Eye Res. 97 (2023) 101206, https://doi.org/10.1016/j.preteyeres.2023.101206.

[16] D. Le, M. Alam, C.K. Yao, J.I. Lim, Y.-T. Hsieh, R.V.P. Chan, D. Toslak, X. Yao, Transfer learning for automated OCTA detection of diabetic retinopathy, Transl. Vision Sci. Technol. 9 (2020) 35, https://doi.org/10.1167/tvst.9.2.35.

[17] Y.-L. Xu, Y. Ma, Q. Zhao, Correlation of glucose and lipid metabolism, renal function and retinopathy in diabetic retinopathy patients using OCTA detection, Am. J. Transl. Res. 16 (2024) 3626–3636, https://doi.org/10.62347/WFUF5719.

[18] T.R.P. Taylor, M.J. Menten, D. Rueckert, S. Sivaprasad, A.J. Lotery, The Role of the Retinal Vasculature in Age-Related Macular Degeneration: a Spotlight on OCTA, Eye 38 (2024) 442–449, https://doi.org/10.1038/s41433-023-02721-7.

[19] A. Heinke, H. Zhang, K. Broniarek, K. Michalska-Małecka, W. Elsner, C.M. B. Galang, D.N. Deussen, A. Warter, F. Kalaw, I. Nagel, A. Agnihotri, N.N. Mehta, J. E. Klaas, V. Schmelter, I. Kozak, S.L. Baxter, D.-U. Bartsch, L. Cheng, C. An, T. Nguyen, W.R. Freeman, Cross-instrument optical coherence tomography-angiography (OCTA)-based prediction of age-related macular degeneration (AMD) disease activity using artificial intelligence, Sci. Rep. 14 (2024) 27085, https://doi.org/10.1038/s41598-024-78327-0.

[20] D.N. Sayah, I. Garg, R. Katz, Y. Zhu, Y. Cui, R. Zeng, R. Tandias, J.Y. Moon, F. Vingopoulos, H.E. Wescott, G. Baldwin, K. Wang, T. Elze, C.A. Ludwig, D. G. Vavvas, J.W. Miller, D. Husain, L.A. Kim, N.A. Patel, J.B. Miller, Characterizing macular neovascularization in myopic macular degeneration and age-related macular degeneration using swept source OCTA, Clin. Ophthalmol. 17 (2023) 3855–3866. https://www.tandfonline.com/doi/abs/10.2147/OPTH.S440575.

[21] F. Corvi, M. Cozzi, A. Invernizzi, L. Pace, S.R. Sadda, G. Staurenghi, Optical coherence tomography angiography for detection of macular neovascularization associated with atrophy in age-related macular degeneration, Graefes Arch. Clin. Exp. Ophthalmol. 259 (2021) 291–299, https://doi.org/10.1007/s00417-020-04821-6.

[22] Y. Hirano, N. Suzuki, T. Tomiyasu, R. Kurobe, Y. Yasuda, Y. Esaki, T. Yasukawa, M. Yoshida, Y. Ogura, Multimodal imaging of microvascular abnormalities in retinal vein occlusion, J. Clin. Med. 10 (2021) 405, https://doi.org/10.3390/jcm10030405.

[23] H.L. Rao, Z.S. Pradhan, M.H. Suh, S. Moghimi, K. Mansouri, R.N. Weinreb, Optical coherence tomography angiography in glaucoma, J. Glaucoma 29 (2020) 312, https://doi.org/10.1097/IJG.0000000000001463.

[24] J.-H. Wu, S. Moghimi, T. Nishida, V. Mohammadzadeh, A. Kamalipour, L. M. Zangwill, R.N. Weinreb, Association of macular OCT and OCTA parameters with visual acuity in glaucoma, Br. J. Ophthalmol. 107 (2023) 1652–1657, https://doi.org/10.1136/bjo-2022-321460.

[25] Y. Shiga, T. Nishida, J.W. Jeoung, A. Di Polo, B. Fortune, Optical coherence tomography and optical coherence tomography angiography: essential tools for detecting glaucoma and disease progression, Front. Ophthalmol. 3 (2023), https://doi.org/10.3389/fopht.2023.1217125.

[26] L. Huang, Y. Fu, R. Chen, S. Yang, H. Qiu, X. Wu, S. Zhao, Y. Gu, P. Li, SNR-adaptive OCT angiography enabled by statistical characterization of intensity and decorrelation with multi-variate time series model, IEEE Trans. Med. Imag. 38 (2019) 2695–2704, https://doi.org/10.1109/TMI.2019.2910871.

[27] R.K. Wang, L. An, Doppler optical micro-angiography for volumetric imaging of vascular perfusion in vivo, Opt. Express, OE 17 (2009) 8926–8940, https://doi.org/10.1364/OE.17.008926.

[28] R.K. Wang, L. An, P. Francis, D.J. Wilson, Depth-resolved imaging of capillary networks in retina and choroid using ultrahigh sensitive optical microangiography, Opt. Lett. 35 (2010) 1467, https://doi.org/10.1364/OL.35.001467.

[29] Z. Xie, N. Zeinstra, M.A. Kirby, N.M. Le, C.E. Murry, Y. Zheng, R.K. Wang, Quantifying microvascular structure in healthy and infarcted rat hearts using optical coherence tomography angiography, IEEE Trans. Med. Imag. 43 (2024) 2878–2887. https://ieeexplore.ieee.org/abstract/document/10488137.

[30] W. Shi, C. Chen, C.R. Pasarikovski, W. Gao, V.X. Yang, Differential phase standard-deviation-based optical coherence tomographic angiography for human retinal imaging in vivo, Appl. Opt. 58 (2019) 3401–3409. https://opg.optica.org/abstract.cfm?uri=ao-58-13-3401.

[31] W. Shi, W. Gao, C. Chen, V.X.D. Yang, Differential standard deviation of log-scale intensity based optical coherence tomography angiography, J. Biophot. 10 (2017) 1597–1606, https://doi.org/10.1002/jbio.201600264.

[32] Y. Jia, O. Tan, J. Tokayer, B. Potsaid, Y. Wang, J.J. Liu, M.F. Kraus, H. Subhash, J. G. Fujimoto, J. Hornegger, Split-spectrum amplitude-decorrelation angiography with optical coherence tomography, Opt. Express 20 (2012) 4710–4725. https://opg.optica.org/abstract.cfm?uri=oe-20-4-4710.

[33] A. Mariampillai, B.A. Standish, E.H. Moriyama, M. Khurana, N.R. Munce, M.K. K. Leung, J. Jiang, A. Cable, B.C. Wilson, I.A. Vitkin, V.X.D. Yang, Speckle variance detection of microvasculature using swept-source optical coherence tomography, Opt. Lett., OL 33 (2008) 1530–1532, https://doi.org/10.1364/OL.33.001530.

[34] X. Ye, H. Zhang, P. Xiao, G. Wang, X. Hu, C. Yan, F. Li, Y. Hu, L. Su, J. Luo, J. Yuan, F. Wen, W. Chi, Microvasculature features of Vogt-Koyanagi-Harada disease revealed by widefield swept-source optical coherence tomography angiography, Front. Med. 8 (2021), https://doi.org/10.3389/fmed.2021.719593.

[35] S. Wu, R. Okada, Y. Liu, Y. Fang, F. Yan, C. Wang, H. Li, H. Kobayashi, Y. Chen, Q. Tang, Quantitative analysis of vascular changes during photoimmunotherapy using speckle variance optical coherence tomography (SV-OCT), Biomed. Opt. Express, BOE 12 (2021) 1804–1820, https://doi.org/10.1364/BOE.419163.

[36] C. Blatter, J. Weingast, A. Alex, B. Grajciar, W. Wieser, W. Drexler, R. Huber, R. A. Leitgeb, In situ structural and microangiographic assessment of human skin lesions with high-speed OCT, Biomed. Opt. Express, BOE 3 (2012) 2636–2646, https://doi.org/10.1364/BOE.3.002636.

[37] Y. Zhang, W. Gao, L. Zhang, W. Shi, Handheld optical coherence tomography based on logarithmic compensation and motion threshold, Chin. J. Lasers 45 (2018) 1107002, https://doi.org/10.3788/CJL201845.1107002.

[38] J. Shi, Z. Guo, C. Dong, F. Xing, Y. Di, Z. Gan, C. Liu, J. Liu, H. Zhu, High-contrast optical coherence tomography angiography based on normalized complex decorrelation, IEEE Photon. Technol. Lett. 36 (2024) 799–802, https://doi.org/10.1109/LPT.2024.3400842.

[39] W. Yi, K. Hu, Y. Wan, F. Wu, W. Song, A high-speed near-infrared optical coherence tomography angiography system for mouse retina, J. Lumin. 270 (2024) 120550, https://doi.org/10.1016/j.jlumin.2024.120550.